Article

Ab Initio Study of Hydrogen Niobate HNbO₃: Structural, Thermodynamic, Dielectric, and Optical Properties

Lingyuan Gao,[†] Robert B. Wexler,[†] Ruixiang Fei,[†] and Andrew M. Rappe*

Read Online

ACCESS | 📊 Metrics & More | 📖 Article Recommendations

HNbO₃ structure
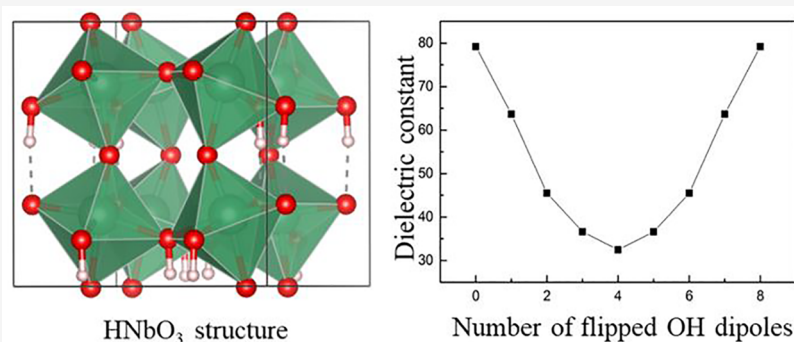
ABSTRACT: Using first-principles calculations, we study the ground-state structure of bulk proton-exchanged lithium niobate, which is also called hydrogen niobate and is widely used in waveguides. Thermodynamics helps to establish the most favorable nonpolar surface as well as the water-deficient and water-rich phases under different ambient conditions, which we refer to as "dehydrated" and "rehydrated" phases, respectively. We compute the low-frequency dielectric response and the optical refractive indices of hydrogen niobate in different phases. The dielectric constant is greatly enhanced compared to lithium niobate. At shorter wavelengths, the refractive indices vary between each phase and have a sharp contrast to lithium niobate. Our study characterizes the structures and thermal instabilities of this compound and reveals its excellent dielectric and optical properties, which can be important in the future application in waveguides.

INTRODUCTION

Lithium niobate, LiNbO₃, is a human-made ferroelectric material.[1] With a high phase transition temperature close to its melting point (1480 K), it exhibits excellent piezoelectric, electro-optic, photorefractive, and nonlinear optical properties. These advantages make LiNbO₃ widely used in optical phase modulators,[2,3] holographic memory storage,[4,5] and nonlinear frequency converters.[6,7] Owing to its large electro-optic coefficient, high refractive index, and wide frequency range with high optical transparency, nowadays LiNbO₃ has become one of the most promising platforms for integrated photonics.[8]

Currently, there are two main methods to integrate LiNbO₃-based optical waveguides: (1) titanium in-diffusion,[9,10] and (2) proton exchange.[11] The first approach has advantages of small effective diffusion length and good confinement of both ordinary and extraordinary waves (increase of refractive indices $\delta n \approx 0.04$).[9,12,13] Alternatively, proton exchange is more straightforward in that by immersing LiNbO₃ in an acid such as benzoic acid, Li⁺ ions diffuse out of the crystal, while H⁺ ions diffuse into the crystal.[11] The replacement of Li⁺ with H⁺ usually takes place up to several microns from the surface of LiNbO₃,[14] and the change of the composition in this surface

layer induces a jump of refractive index relative to the part below. Compared to titanium in-diffusion, proton-exchange gives a higher refractive index change for the extraordinary wave ($\delta n_e \approx 0.12$).[11,15] The proton exchange is usually followed by an annealing step at a controllable duration and temperature, called as "annealing proton exchange" (APE), which can restore electro-optical effect and nonlinear coefficients and lower propagation loss.[16,17] Sometimes, a reverse proton exchange (RPE) procedure is also adopted by re-exchanging the protons near the surface back to Li⁺ ions, thereby burying exchanged waveguides in eutectic or pure LiNbO₃.[18,19] RPE can increase depth index profile symmetrization and reduce fiber waveguide coupling loss.[17,20]
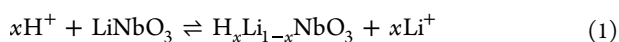
Generally, proton exchange can be viewed as a chemical reaction,[21] expressed as

$$x\text{H}^+ + \text{LiNbO}_3 \rightleftharpoons \text{H}_x\text{Li}_{1-x}\text{NbO}_3 + x\text{Li}^+ \qquad (1)$$
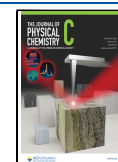
$\text{H}_x\text{Li}_{1-x}\text{NbO}_3$ is a complex product, and there can be up to seven different crystallographic phases, highly dependent on the orientation of crystal cut (X-, Y-, or Z-) and the proton concentration x.[16,17,19,22−24] As a function of x in the exchange layer, lattice parameters can change abruptly and there can be sudden jumps between different crystal phases.[16,17,19,22−24] This induces an abrupt change of local refractive index and is detrimental to the performance of the waveguide. Therefore, it is vital to characterize the structural and optical properties of $\text{H}_x\text{Li}_{1-x}\text{NbO}_3$.

In this work, instead of examining all the possible phases with different proton concentration x, we focus on hydrogen niobate HNbO_3, which can be synthesized from LiNbO_3 via ion exchange when Li^+ ions are fully replaced by H^+ ions.[25] The forward conversion from LiNbO_3 to HNbO_3 is more complete than the backward conversion from HNbO_3 to LiNbO_3 in concentrated acid treatment.[21] X-ray diffraction shows that at room temperature 300 K, HNbO_3 has an $Im\overline{3}$ space group, and it is a cubic perovskite with corner-sharing NbO_6 units. The refined lattice constant is $a = 7.645$ Å.[26−28] Nevertheless, the positions of H atoms are not well located, and previous studies showed that they are statistically distributed on two types of positions.[26] Nuclear magnetic resonance (NMR) spectra also indicated that protons can easily jump from one oxygen to another unbonded oxygen.[29]

Using first-principles calculations, we first search for the ground-state structure using an automatic algorithm. As we find, the ground-state structure is highly polarized, with all OH^- groups aligned along the same direction. These OH^- groups can be flipped with an external electric field at a small energy cost. From the predicted bulk structure, we establish the most stable nonpolar HNbO_3 surface and identify the corresponding passivation layers and adsorbates in ambient environment. The following thermodynamic studies show that water can be easily desorbed and reabsorbed into HNbO_3 under different ambient conditions, which leads to the formation of the water-deficient ("dehydrated") or water-rich ("rehydrated") phases. We finally study the dynamic low-frequency dielectric response and optical refractive indices of HNbO_3 in different phases. The dielectric constant is almost doubled in polar HNbO_3 compared to that of LiNbO_3, and the refractive indices also differ from LiNbO_3 and vary between different phases.

■ STRUCTURE EXPLORATION OF HYDROGEN NIOBATE

Ground-State Structure of Bulk Hydrogen Niobate.
According to ref 26, the neutron spectrum of HNbO_3, measured at 4 K, remains similar to that measured at room temperature, indicating that the unit cell is cubic at both temperatures. Thus, we take the experimentally observed room-temperature HNbO_3 structure as the starting point of our calculation, as shown in Figure 1a.[26] The cubic unit cell contains 8 NbO_6 octahedra, and the tilting pattern is $a^0a^0c^+$. We note that this is a conventional cell, and the primitive cell has 20 atoms. A total of 48 available sites are available to be occupied by 8 H atoms, which generates 377,348,994 configurations in total. With such a huge number, we carry out a pseudorandom approach with the help of density functional theory (DFT) to search for the ground-state-zero-temperature structure.
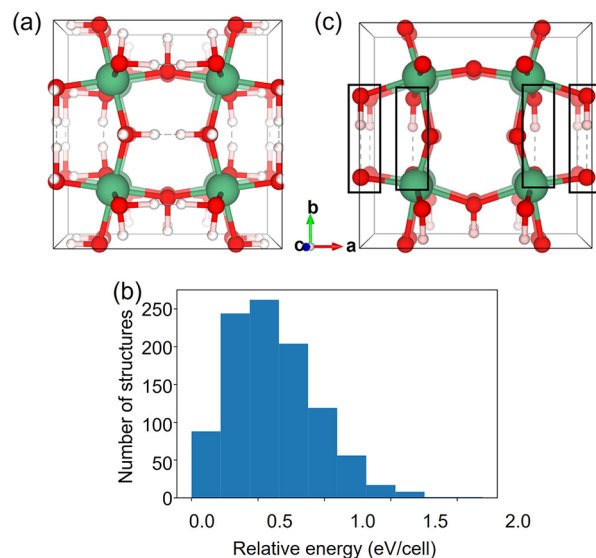

Figure 1. (a) Experimental crystal structure of HNbO_3.[26] White, green, and red denote H, Nb, and O atoms, respectively. There are 48 available positions to occupy 8 H atoms. (b) Count distribution of relative energies of 1,000 candidate structures. (c) Computed ground-state structure of HNbO_3. Compared with (a), we see that particular positions have been determined by energy minimization for the 8 H atoms. Four O−O bridges are highlighted by black squares. Four protons around $y = 0.5$ are close to the midpoint of these O−O bridges.

We establish three rules as the constraints of our searching algorithm: (1) The number of H atoms bonded to each O atom should be no more than one. This corresponds to the condition that the formation of H_2O is unfavorable. (2) H−H distances should be longer than 1 Å so as to avoid the unfavorable formation of H_2 in HNbO_3. (3) The number of OH^- bonded to each Nb atom should not exceed three, to ensure that each Nb is locally charge balanced. With these constraints, we randomly generate 1000 structures by dropping 8 H atoms on available positions in the cubic cell with the experimental lattice parameters (Figure 1a). We then conduct geometric relaxations for all 1000 structures including changing the shape and volume of the cell and computing their total energies. Our DFT calculations are performed using the Quantum Espresso package,[30] and we use norm-conserving pseudopotentials generated by the OPIUM package.[31] The generalized gradient approximation (GGA) exchange-correlation functional[32] is adopted.

Figure 1b shows the count distribution of relative energies of all 1,000 structures. The total energy per conventional cell varies in a 1.8 eV/cell range with the median energy of 0.59 eV. Energetically, many configurations are close to the ground-state structure. The lowest-energy structure of HNbO_3 is shown in Figure 1c. It is triclinic but close to tetragonal, with $a = 7.67$ Å, $b = 7.33$ Å, $c = 7.68$ Å, $\alpha = 90.002°$, $\beta = 89.722°$, and $\gamma = 90.000°$. The tilting pattern is $a^0a^0c^+$, consistent with the experimentally observed structure. In each NbO layer, four H atoms are attached on four different O atoms in a symmetric pattern, and each proton is close to the midpoint of the O−O bridge along b ([010]) direction. In this way, eight OH^- groups are aligned in parallel and maximize the polarization of the system. All atomic positions have been reported in Table 1. However, since many configurations are thermally accessible according to Figure 1b, the OH^- groups can be very

Table 1. Atomic Positions in the Conventional, Pseudo-Cubic Cell Shown in Figure 1c[a]

atom	fractional coordinate (x, y, z)	atom	fractional coordinate (x, y, z)
H1	(0.4916, 0.0335, 0.7339)	O3	(0.4966, 0.8276, 0.7418)
H2	(0.4913, 0.0334, 0.2722)	O4	(0.4938, 0.1744, 0.2667)
H3	(0.252, 0.5331, 0.503)	O5	(0.2481, 0.6743, 0.5055)
H4	(0.2305, 0.0331, 0.0031)	O6	(0.237, 0.828, 0.0081)
Nb1	(0.2316, 0.7768, 0.2626)	O7	(0.2346, 0.1743, 0.0006)
Nb2	(0.2203, 0.2444, 0.7326)	O8	(0.2457, 0.3279, 0.498)
Nb3	(0.2627, 0.7444, 0.7735)	O9	(0.1852, 0.9967, 0.6978)
Nb4	(0.2513, 0.2768, 0.2434)	O10	(0.2977, 0.4967, 0.8082)
O1	(0.4891, 0.1744, 0.7394)	O11	(0.1803, 0.0113, 0.3131)
O2	(0.4863, 0.8276, 0.2643)	O12	(0.3026, 0.5112, 0.193)

[a]Positions for 20 atoms (x, y, z) are listed in the table and positions for the other 20 atoms are (x, y, z) + (0.5, 0.5, 0.5).

disordered, and different orientations of OH⁻ will induce a change of the polarization of the system. By carrying out nudged elastic band (NEB) calculations, we calculate the energy barrier for flipping OH⁻ groups, which can be completed by displacing a H atom from one side of the O–O bridge to the other side. As shown in Figure 2, to flip the first OH⁻ group (at $y = 0.5$) requires an energy about 0.3 eV (Image 9), and then to flip the second OH⁻ group (at $y = 1$) requires an energy about 0.45 eV (Image 18). The energy barrier is much smaller compared to the energy of H-bond and OH-bond, and that indicates that the polarization of HNbO₃ can be easily switched with a small electric field. Comparing the total energies, we find that one- and two–OH⁻ flipped structures are 0.3 eV and 50 meV higher than the ground-state polar HNbO₃. This demonstrates that HNbO₃ with various OH⁻ orientations and polarizations widely exist in nature. As

we see from our benchmark calculations, the ground-state structure of HNbO₃ is little affected by the vdW correction.

Stable Nonpolar Surface of Hydrogen Niobate. To date, there have not been many studies about HNbO₃ surfaces. The Bravais–Friedel–Donnay–Harker (BFDH) theory states that the morphological importance of a particular facet is proportional to the interplanar spacing along the direction normal to this facet.[33−35] Since in HNbO₃ three lattice constants are similar, the probabilities of the formation of (± 100), (0 ± 10), and (00 ± 1) surfaces are approximately equal. Also, since a and c directions are symmetrically equivalent, we only consider (0 ± 10) and (00 ± 1) surfaces. Figure 3a shows that the (001) and (010) surfaces are different in terms of their polarities: The OH⁻ groups in the (001) surface point to the left within the surface plane, while dipoles in the (010) surface point downward normal to the surface. $[(OH)_2O_2]^{-6}$ and $[H_2Nb_4O_8]^{+6}$ layers are alternately stacked along the [001] direction, while $[H_4O_4]^{-4}$ and $[Nb_4O_8]^{+4}$ layers are stacked along the [010] direction. Below, we only consider the nonpolar (001) surface.

As shown in Figure 3a, the dangling OH⁻ groups and O²⁻ ions on the top of (001) surface can induce dipoles that destabilize the surface. These surface dipoles can be chemically passivated by ambient H₂O and O₂. After considering thermodynamics of 25 possible passivation schemes, we identify two most stable surfaces:

$$HNbO_3(001): H_2Nb_4O_8 + OH^- + O^{2-} + 2H_2O$$

$$HNbO_3(001): H_2Nb_4O_8 + 3OH^- + H_2O \tag{2}$$
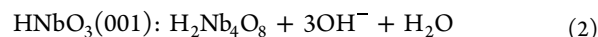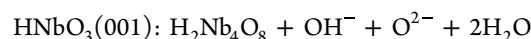
Here, H₂Nb₄O₈ refers to the prepassivation surface layer, and adsorbates include OH⁻, O²⁻, and H₂O. Structures of the two passivated surface layers are illustrated in Figure 3b. Adsorbates sitting on Nb⁵⁺ sites form square H-bonding
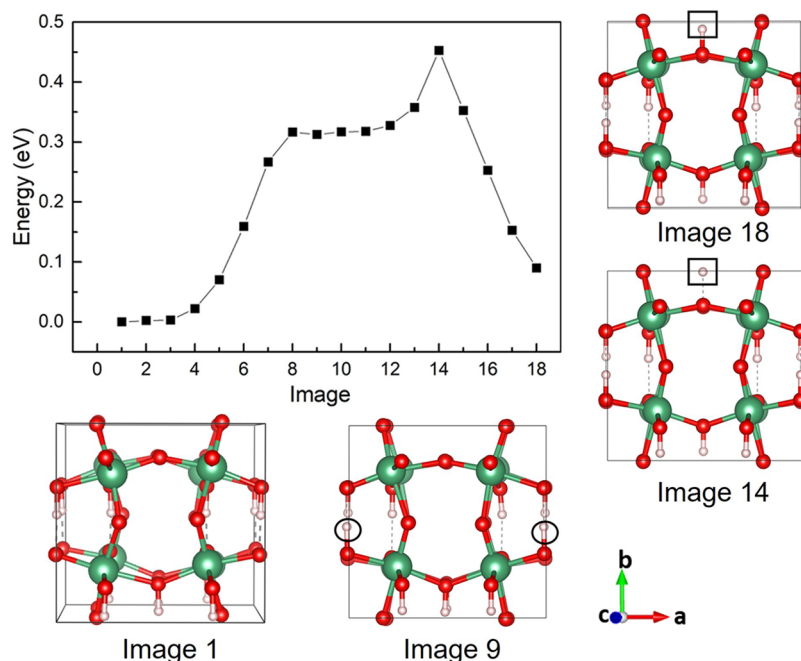

Figure 2. Energy barrier for flipping OH⁻ groups by the NEB calculation. Structures of one- and two-OH⁻ flipped structures are given (images 9 and 18, respectively). Flipping OH⁻ groups can be accomplished by displacing H atoms from one side to the other side of the O–O bridge along the b ([010]) direction. In image 9, black circles highlight the displaced proton close to $y = 0.5$. In images 14 and 18, black square highlights the displaced proton close to $y = 1$.
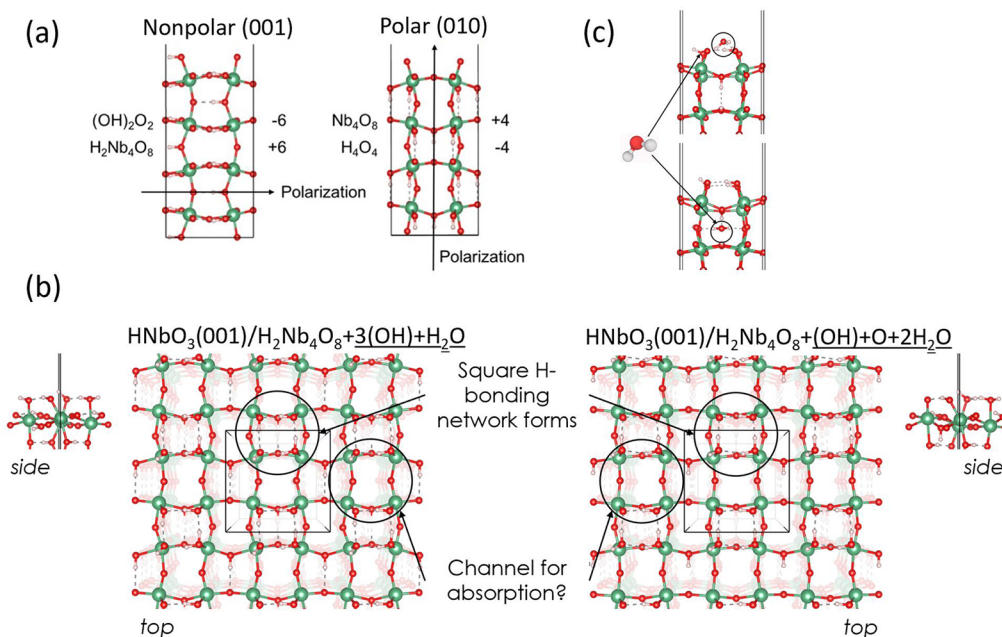
Figure 3. (a) Slab models of nonpolar (001) and polar (010) $HNbO_3$ surfaces. Components and charges of each layer are different. (b) Two most stable $HNbO_3$ (001) passivated layers with different adsorbates. The planarities are also shown from the side view. (c) Illustration of an adsorption of an extra H_2O on the surface and absorption of an extra H_2O through $HNbO_3$(001) surface.

networks, surrounded by Nb_4 squares. Binding energies of H_2O to the surface are 1.08 and 1.24 eV for $2H_2O$ and $1H_2O$ adsorbed, respectively. Large binding energies suggest H_2O binds strongly to the (001) surface, and the Nb^{5+} sites without OH^- and O^{2-} should be saturated with H_2O. As a result, these sites are possible channels for the absorption and desorption of water. These two configurations have the lowest surface energies, which are 0.18 and 0.17 J/m^2 for $2H_2O$ and $1H_2O$ adsorbed, respectively. As a comparison, for niobate-deficient $(HNbO_3(001): H_2Nb_4O_8 - NbO)$ layer, the surface energy is 0.3 J/m^2.

While these two surfaces are thermodynamically preferred, other surfaces can also be accessed kinetically, albeit transiently. Here, we considered two (of many) possible classes of kinetic events: an extra H_2O adsorption to the adsorbates on top of $H_2Nb_4O_8$ and H_2O absorption in the bulk. As shown in Figure 3c, the H-bonding network from the adsorbed OH^- and H_2O provides an adsorption site for an extra H_2O, and the adsorption energy is 0.66 eV. If we leave the H_2O beneath the surface layer $H_2Nb_4O_8$, representing the H_2O is transported through the surface and fully absorbed in the bulk region, the absorption energy is −1.28 eV. The negative number suggests that the surface is not water permeable, and H_2O molecules prefer to be adsorbed on the surface.

THERMODYNAMIC STABILITY OF HYDROGEN NIOBATE

In $HNbO_3$, apart from adsorption, H_2O can also escape from $HNbO_3$ via the pathway

$$2HNbO_3 \rightleftharpoons H_2O + Nb_2O_5 \qquad (3)$$

Nb_2O_5, a stable bulk niobium oxide, is the other product of this decomposition. By releasing H_2O, this can be thought as a dehydration process. Figure 4 shows the Gibbs free energy $G = H - TS$ of the complete dehydration as a function of
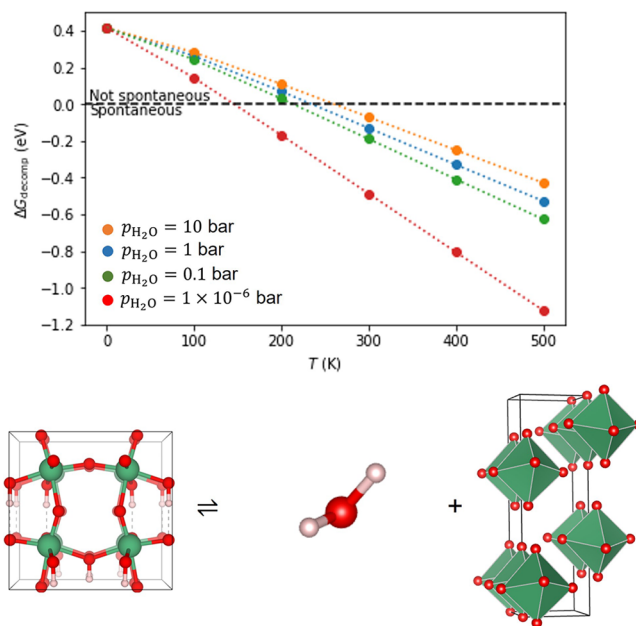

Figure 4. Gibbs free energy diagram of $HNbO_3$ for the complete dehydration into Nb_2O_5 under different temperatures and pressures of H_2O. The process is illustrated on the bottom.

temperature and pressure of H_2O. For all pressures, when the temperature increases, dehydration becomes more spontaneous. The transition between nonspontaneous and spontaneous dehydration occurs between 150 and 250 K, depending weakly on water vapor. The figure reveals that near or above room temperature, $HNbO_3$ is expected to decompose spontaneously. In the transition region, the contribution from entropy TS is more significant than the contribution from enthalpy H. When the pressure of H_2O decreases from 1 bar to 1×10^{-6} bar, the transition temperature will also decrease, in line with Le Châtelier's principle. As Nb^{5+} cannot
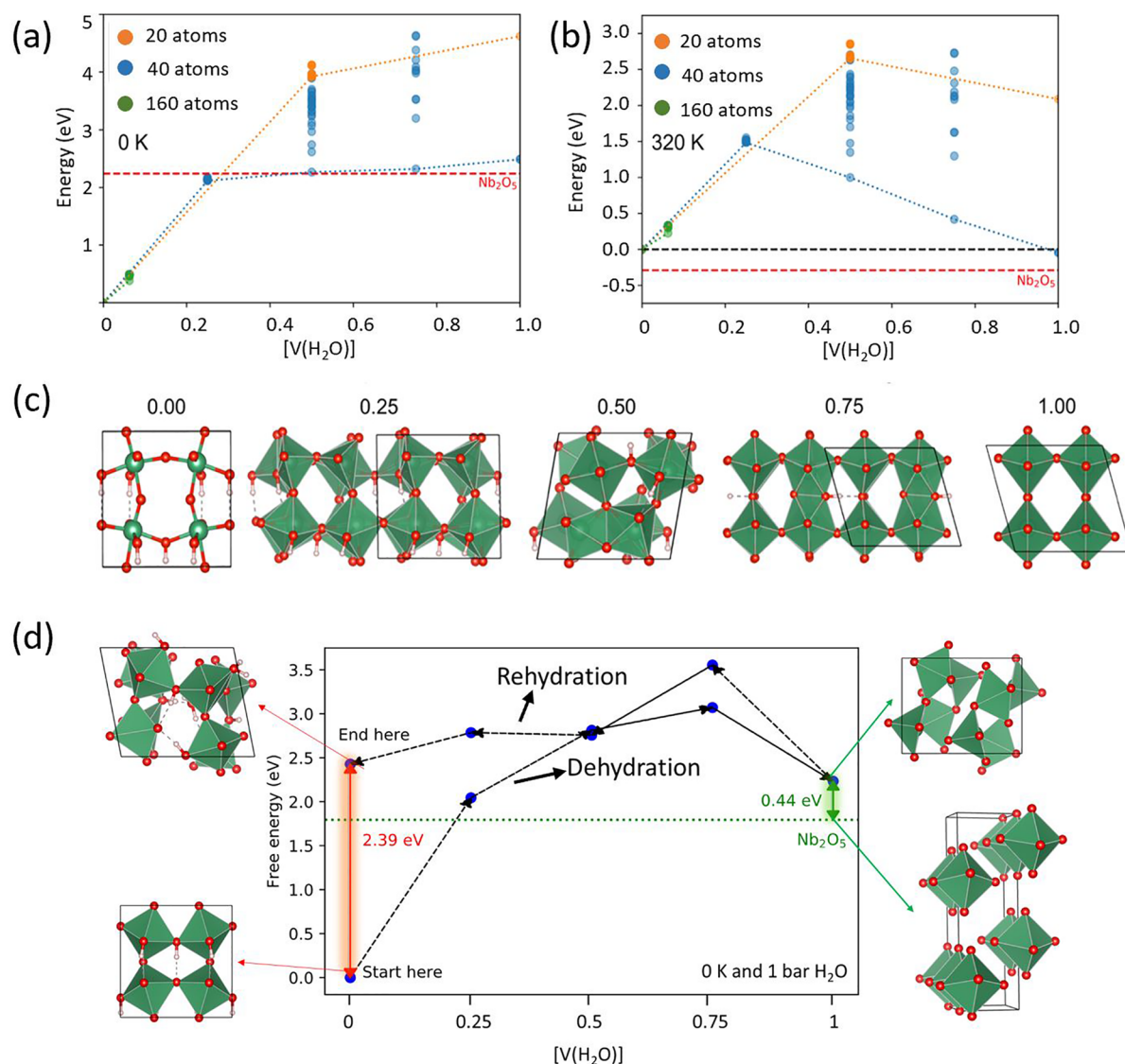
Figure 5. (a) Energy profile for partial HNbO$_3$ dehydration at 1 bar and 0 K. Orange, blue, and green correspond to a 20-atom primitive cell, 40-atom conventional cell, and 160-atom $2 \times 2 \times 2$ supercell, respectively. Dotted lines connect minimum energy points at different x. As a reference, the energy of bulk Nb$_2$O$_5$ is denoted with the red dashed line. (b) Similar to (a), but the energy profile is at room temperature 320 K. (c) Structural changes of HNbO$_3$ at different partial dehydration conditions at 0 K. (d) A complete dehydration–rehydration hysteresis of HNbO$_3$ in a 40-atom conventional cell when the water is added back to the final dehydrated structure at 320 K. Rehydration gives a different HNbO$_3$ structure at the end from the ground state.

be further oxidized, we consider that the adsorption of other gas molecules in ambient environment will have limited effect on stabilities of the products.

At equilibrium, the dehydration process can be partial, i.e.,

$$HNbO_3 \rightleftharpoons 2xH_2O + H_{1-x}NbO_{3-2x} \qquad (4)$$
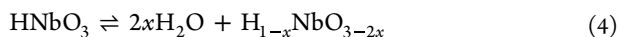
where $0 < x < 1.0$. Due to the limit of the size of the supercell, we model a few possible values of x. For example, we can model $x \in \{0, 0.50, 1.0\}$ in a 20-atom primitive cell, and we can model $x \in \{0, 0.25, 0.50, 0.75, 1.0\}$ in a 40-atom conventional cell. In a 160-atom $2 \times 2 \times 2$ supercell, we can model $0.0 < x < 1.0$ in increments of 0.0625. The results of partial dehydration calculations for different x and temperatures are shown in Figure 5. At 0 K (Figure 5a), the partial dehydration of HNbO$_3$ is unfavorable, as more than 2 eV per cell is needed to achieve 25% dehydration. As illustrated in Figure 5c, the structure remains approximately the same when

$x = 0.25$ and the tilting pattern is mostly retained. When $x > 25\%$, dehydration is more favorable with a lower cost of energy, and structural change is more dramatic with an orthorhombic-monoclinic phase transition at $x = 0.50$. Edge-sharing Nb−O polyhedra are formed, resembling bulk Nb$_2$O$_5$. The final structure at $x = 1.0$ is slightly higher in energy than bulk Nb$_2$O$_5$, and that is likely due to the absence of thermal energy for overcoming kinetic barriers to Nb$_2$O$_5$. At 320 K (Figure 5b), the partial dehydration is still unfavorable from the intact HNbO$_3$ to 25% dehydration but now it requires 0.5 eV less compared to the dehydration at 0 K. Beyond 25%, dehydration is downhill in energy, indicating that once the system reaches this turning point, it will be spontaneously decomposed to Nb$_2$O$_5$.

Next, we add the water back to the final dehydrated loop to form a complete dehydrate-rehydrate hysteresis. Results are shown in Figure 5d; clearly, the rehydration pathway gives

different products from the dehydration pathway. The $HNbO_3$ structure can be gradually recovered, and the final rehydrated structure is 2.5 eV higher compared to the polar $HNbO_3$, demonstrating that the rehydrated $HNbO_3$ is less stable.

To make the analysis more complete, we also consider the dehydration at the surface of $HNbO_3$. Figure 6a shows the top
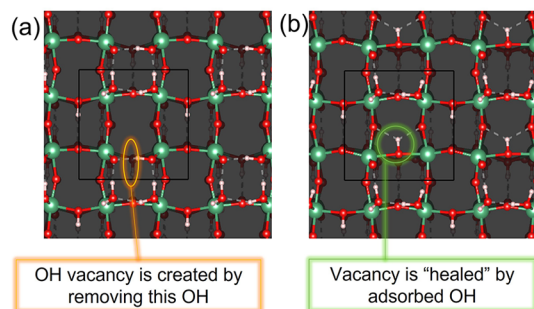

Figure 6. (a) The most stable dehydrated nonpolar $HNbO_3$ (001) surface. An H_2O vacancy is created by removing an OH^- highlighted by the orange circle, and a H atom below the black plane. (b) After performing structural relaxation, OH vacancy is healed by the migration of adsorbed OH^- from the nearby Nb^{5+} site, and H vacancy is also healed by extra H ions.

view of the most stable dehydrated nonpolar $HNbO_3$(001) surface, built from the $2H_2O$-adsorbed surface shown in Figure 3b. H_2O vacancies are created by removing OH^- ions on the top $H_2Nb_4O_8$ layer (indicated by the orange circle) and removing hydrogen atoms below (beneath the black plane, not visible here). In fact, as we will show in a future work, the kinetic barrier for H diffusion in $HNbO_3$ is very small (~0.1 eV), so H vacancies can readily hop between oxygen atoms. Given structural relaxation, extra OH^- ions adsorbed at nearby Nb^{5+} sites move to OH vacancy sites on the top $H_2Nb_4O_8$ layer, and that effectively heals the Nb−OH−Nb link presented before surface dehydration. H vacancy below the surface plane is also healed by extra H ions from proton sources. In this way, $HNbO_3$ can recover its surface structure in low humidity environments.

Based on these calculations, we propose the hypothesis for the optical performance of $HNbO_3$-based materials under different environmental conditions (see Figure 7). Under a

back pressure of H_2O, the surface will be saturated with H_2O. If there are any OH or H vacancies, they will be immediately healed by the adsorbates. If $HNbO_3$ is placed in vacuum, dehydration will occur, and that will cause a drastic change in local crystal structure and a downgrade in performance. Finally, if the dehydrated surface is placed back in a humid environment, H_2O will be readsorbed on the surface and heal surface vacancy sites.

◼ DIELECTRIC AND OPTICAL PROPERTIES OF HYDROGEN NIOBATE

Low-Frequency Dielectric Response of Hydrogen Niobate. As the hydrogen niobate is the exchange product of lithium niobate, we first calculate and compare their dielectric properties. From the linear response theory,[36] the macroscopic low-frequency dielectric permittivity tensor $\epsilon_{\alpha\beta}(\omega)$ can be written as the sum of electronic ($\epsilon_{\alpha\beta}^{\infty}$) and ionic contributions:

$$\epsilon_{\alpha\beta}(\omega) = \epsilon_{\alpha\beta}^{\infty} + \frac{4\pi}{\Omega}$$
$$\times \sum_m \frac{\left(\sum_{\kappa\mu} Z_{\kappa,\alpha\mu}^* U_{m,\mathbf{q}=0}(\kappa,\mu)\right)\left(\sum_{\kappa'\nu} Z_{\kappa',\beta\nu}^* U_{m,\mathbf{q}=0}(\kappa',\nu)\right)}{\omega_m^2 - \omega^2}$$

$$(5)$$

where Ω is the volume of the unit cell, $U_{m,\mathbf{q}=0}(\kappa,\mu)$ is the eigen-displacement of phonon mode m at wavevector $\mathbf{q} = 0$, and $Z_{\kappa,\alpha\mu}^*$ is the mode-effective charge vector. Subscripts α, β, μ, and ν denote Cartesian coordinates, and κ denotes atoms. The electronic contribution $\epsilon_{\alpha\beta}^{\infty}$ can be computed as

$$\epsilon_{\alpha\beta}^{\infty} = \delta_{\alpha\beta} - \frac{1}{\pi^2} \int_{BZ} \sum_m^{occ} \langle \mu_{m\mathbf{k}}^{E_\alpha} | i \mu_{m\mathbf{k}}^{E_\alpha} \mathbf{k} \rangle$$

$$(6)$$

where $\mu_{m\mathbf{k}}^{E_\alpha}$ is the first-order derivative of the Bloch wave functions with respect to an electric field along direction α. Using density-functional perturbation theory,[36] we first benchmark our method by computing static ($\omega = 0$) dielectric tensor of rhombohedral $LiNbO_3$. As shown in Table 2, our results are close to previously reported values, and the discrepancy originates from the different density functional we choose. This gives us confidence to compute the dielectric tensor of $HNbO_3$.
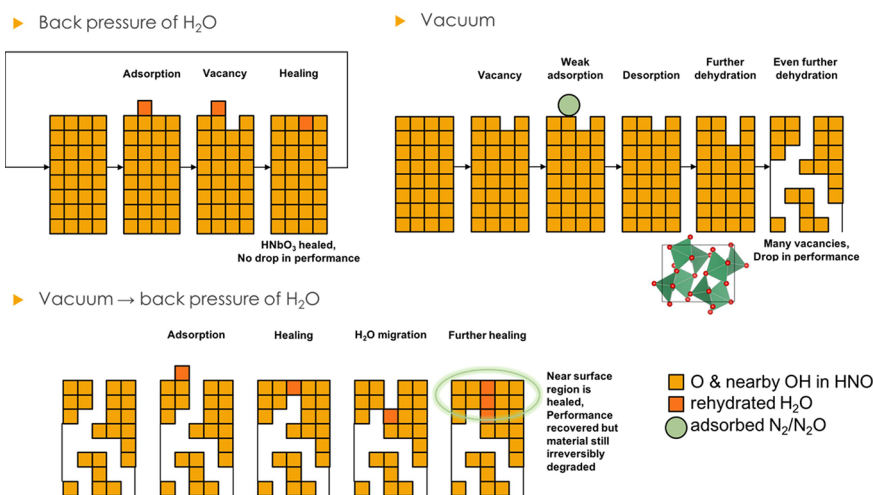

Figure 7. Illustration of the dehydration and rehydration process of $HNbO_3$ surface under different environmental conditions.

Table 2. Static Dielectric Tensor of Rhombohedral LiNbO₃

	ϵ_{xx}^0	ϵ_{yy}^0	ϵ_{zz}^0
calculation[37]	42.4	42.4	29.3
experiment[37]	41.5	41.5	26.0
this work	36.5	36.5	28.7

We calculate the static dielectric tensor of compound $H_xLi_{6-x}Nb_6O_{18}$ by gradually replacing lithium ions with protons in the rhombohedral phase of LiNbO₃. As shown in Figure 8(a), the total ϵ_{zz} is dramatically enhanced with the increasing x. When all Li ions are replaced by protons in the rhombohedral LiNbO₃, static ϵ_{zz} is almost doubled. We note the enhancement mainly comes from the increasingly dominant ionic contribution, while the electronic contribution is kept nearly constant over different proton concentrations. This reveals that the dielectric response is heavily dependent on vibrational motions, dictated by compositions and structures of the system. In Figure 8(b) we show the dynamic low-frequency $\epsilon_{zz}(\omega)$ of the fully exchanged rhomobohedral $H_x Li_{6-x}Nb_6O_{18}$ ($x = 6$). The dielectric tensor varies in a narrow window and is insensitive to the low-frequency driving field, as the field frequency is much smaller than the frequencies of the optical vibrational modes.

Figure 9a shows the dielectric $\epsilon_{zz}(\omega)$ component of the low-frequency dielectric constant tensor of polar HNbO₃. Similar to rhombohedral HNbO₃ (Figure 8b), the total dielectric constant does not change much with the frequency of electric field. At $\omega = 0$, ϵ_{zz} is around 79.25, almost 2.5× larger than that of rhombohedral LiNbO₃. This can be possibly ascribed to the large polarization from eight polarized OH⁻ groups. To test that, Figure 9b shows the change of static dielectric constant by flipping OH⁻ groups. The number on the horizontal axis represents the number of flipped OH⁻ groups. With more OH⁻ flipped, the structure becomes less polarized, and it is fully unpolarized when four OH⁻ groups are flipped. Indeed, we see a dramatic decrease of $\epsilon_{zz}(0)$ with more flipped OH⁻ groups, and the dielectric constant drops to its minimum when four OH⁻ groups are flipped, only about 40% of the initial value. After that, when more OH⁻ groups are flipped, the structure becomes polarized again, though the polarization starts to rise along the opposite direction. Fundamentally there is no difference between OH⁻ groups pointing up or down; therefore we see a symmetric $\epsilon_{zz}(0)$ with the number of flipped OH⁻ groups.

As we discuss in Structure Exploration of Hydrogen Niobate, it is possible that both dehydrated and rehydrated HNbO₃ will form in an ambient environment. In Table 3, we list the diagonal components of the static dielectric tensors of HNbO₃ in all phases. The off-diagonal components are much smaller, so they are not shown. The electronic contribution ϵ^∞ is very similar between these structures and much smaller than the ionic contribution. The largest components are ϵ_{zz} of polar HNbO₃ (79.2) and ϵ_{xx} of rehydrated HNbO₃ (62.6). According to eq 5, frequencies of optical phonon modes ω_m are the decisive factors and they are smaller in polarized HNbO₃, which result in a larger dielectric response.

Refractive Indices of Hydrogen Niobate. To characterize the performance of HNbO₃ in waveguides, we calculate its refractive index as a function of light frequency. The refractive index determines how much the path of light is bent or refracted when light propagates in a material. Theoretically, it can be calculated through the imaginary and real part of the frequency-dependent complex dielectric constant of the materials $\epsilon(\omega)$,

$$n_1(\omega) = \sqrt{\frac{1}{2}\left(\epsilon_1(\omega) + \sqrt{\epsilon_1^2(\omega) + \epsilon_2^2(\omega)}\right)}$$

$$n_2(\omega) = \frac{\epsilon_2^2(\omega)}{\sqrt{2\left(\epsilon_1(\omega) + \sqrt{\epsilon_1^2(\omega) + \epsilon_2^2(\omega)}\right)}} \quad (7)$$

where $n_1(\omega)$ and $n_2(\omega)$ and $\epsilon_1(\omega)$ and $\epsilon_2(\omega)$ are the real and imaginary parts of the refractive index and the complex dielectric constant, respectively. When $\hbar\omega$ falls in the range of visible spectrum, $\epsilon(\omega)$ has a different form from eq 5. From the linear response theory, the imaginary part $\epsilon_2(\omega)$ can be calculated as[38]

$$\epsilon_2(\omega) = \frac{16\pi e^2}{\omega^2} \sum_{c,v} |\langle v|\vec{v}\,|c\rangle|^2 \delta[\hbar\omega - (E_c - E_v)] \quad (8)$$

where $\langle v\vec{v}|c\rangle$ is the dipole matrix element between conduction band c and valence band v. With $\epsilon_2(\omega)$, the real part $\epsilon_1(\omega)$ can be computed via the Kramers−Krönig relation

$$\epsilon_1(\omega) = 1 + \frac{2}{\pi}\mathcal{P}\int_0^\infty d\omega' \frac{\omega'\epsilon_2(\omega)}{\omega'^2 - \omega^2} \quad (9)$$
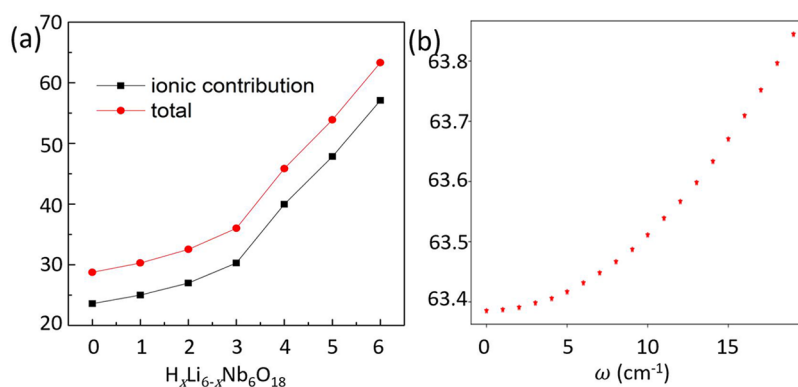

Figure 8. (a) Static dielectric ϵ_{zz} component of the $H_xLi_{6-x}Nb_6O_{18}$ with different x, constructed from the hexagonal conventional cell of rhombohedral LiNbO₃. (b) The dynamic dielectric $\epsilon_{zz}(\omega)$ component of the rhombohedral $H_6Nb_6O_{18}$ with different frequencies of the electric field.
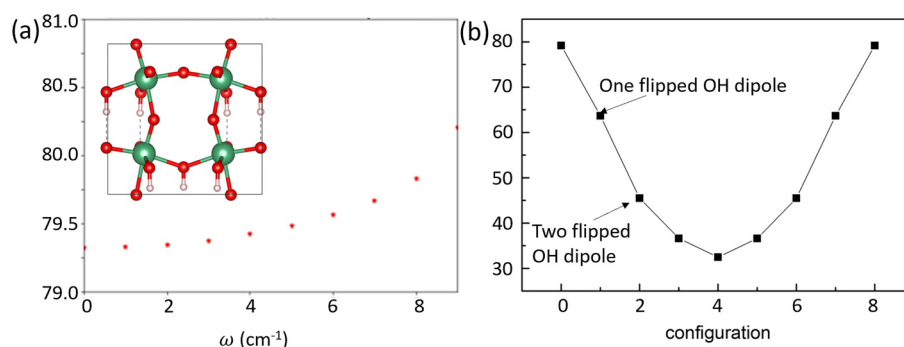
Figure 9. (a) Dynamic dielectric $\epsilon_{zz}(\omega)$ component of the polar $HNbO_3$ with different frequencies of the electric field. (b) Static dielectric $\epsilon_{zz}(\omega = 0)$ with different numbers of flipped OH^- groups.

Table 3. Diagonal Components of Static Dielectric Tensors of Rhombohedral $LiNbO_3$ and Polar, Rehydrated, and Dehydrated $HNbO_3$[a]

	$LiNbO_3$	polar $HNbO_3$	rehydrated $HNbO_3$	dehydrated $HNbO_3$
ϵ_{xx}^{∞}	4.7	5.4	5.5	6.0
ϵ_{yy}^{∞}	4.7	5.4	5.2	5.6
ϵ_{zz}^{∞}	4.8	5.9	4.5	4.5
ϵ_{xx}	36.5	56.4	62.6	34.5
ϵ_{yy}	36.5	56.4	32.2	29.1
ϵ_{zz}	28.7	79.2	25.2	10.1

[a]Electronic contribution ϵ^{∞} of each component is also given.

We first examine the effect of the polarization of light on the refractive index. The polarization direction determines which component of the dipole matrix element is coupled with light. As shown in Figure 10a, for polar $HNbO_3$, when the photon energy is smaller than the band gap, the refractive index for z-polarized light ($n_{xx} \approx 2.4$) is close to indices of x- and y-polarized light ($n_{xx/yy} \approx 2.2$). When $\hbar\omega$ is larger than band gap (2.1 eV), with resonant excitation and optical transitions across the band gap, there is a sharp increase of refractive index for n_{zz}, and it reaches 4.0 when $\hbar\omega = 3.7$ eV. The increase of n_{zz} is more significant than n_{xx} and n_{yy}, consistent with a larger dielectric response ϵ_{zz}^{∞} with purely electronic origin. As a comparison, in $LiNbO_3$, for below-band-gap excitation, the refractive index stays around 2.2 and then it increases to 2.44 when $\hbar\omega = 3.1$ eV.[39] Therefore, the contrast of refractive

indices at the $HNbO_3/LiNbO_3$ interface in waveguides will be strong at shorter wavelengths.

To study the relationship between optical response and macroscopic polarization, we plot refractive indices over the number of flipped OH^- groups. As shown in Figure 10b, the refractive index does not change much with the orientation of OH^- groups. This is because optical excitation characterizes transition between different electronic bands, more correlated with dielectric response from electronic contribution rather than from ionic contribution. As shown in Table 3, the ionic part differs more than the electronic part between different phases of $HNbO_3$. As such, we expect the refractive indices are similar for these OH^--flipped structures.

Figure 11 shows the refractive indices for polar, rehydrated and dehydrated $HNbO_3$. In general, they all exhibit a similar
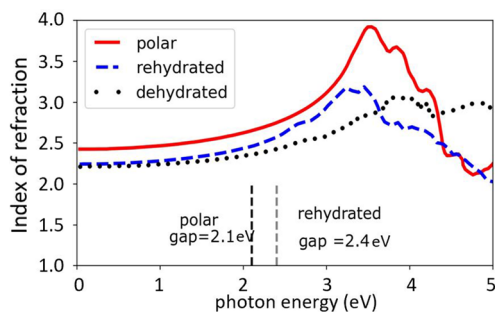

Figure 11. Absolute value of refractive indices ϵ_{zz} of polar, rehydrated, and dehydrated $HNbO_3$.
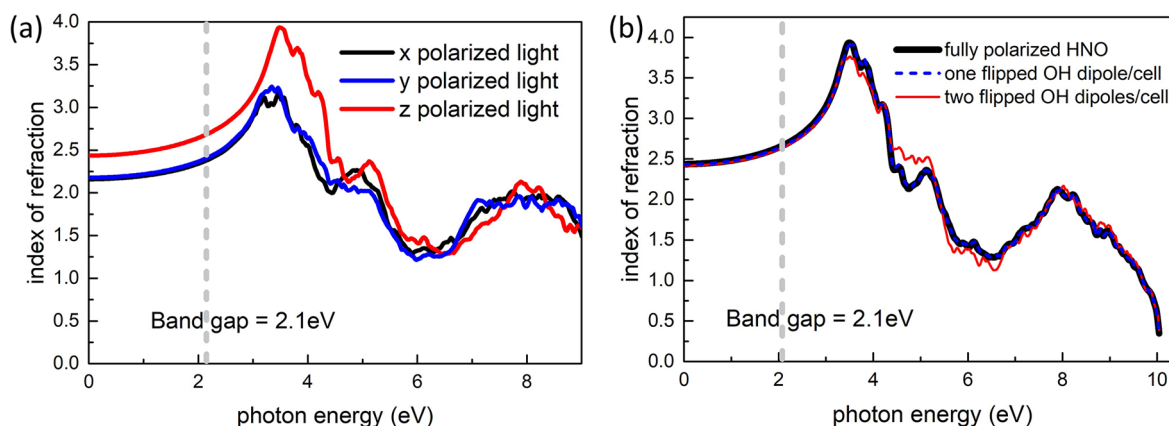

Figure 10. (a) Refractive index of polar $HNbO_3$ with different light polarizations. (b) Refractive indices of $HNbO_3$ with different numbers of flipped OH^- groups.

tendency with the change of photon energy. Below band gap, ϵ_{zz} of polar HNbO$_3$ is 0.2 higher than that of rehydrated and dehydrated HNbO$_3$. Above band gap, ϵ_{zz} is much larger in polar HNbO$_3$ (4.0) than in the other two phases (3.0), and they peak at different photon energies. In dehydrated HNbO$_3$, peak frequencies of n_{xx}, n_{yy} and n_{zz} are also not aligned and vary between 3 and 4 eV (not shown here). As a consequence, when light propagates in areas where all three phases coexist or get mixed, the propagation will be inhomogeneous due to the phase mismatch between light beams.

CONCLUSION

In conclusion, by performing first-principles calculations, we study the ground-state structure of bulk hydrogen niobate and related surfaces. Thermodynamics characterizes the dehydration and rehydration processes of polar hydrogen niobate under different ambient conditions. We further study its low-frequency dielectric response and optical refractive indices in different phases. Our study shows that hydrogen niobate exhibits excellent chemical and physical properties and is promising for the future application of photonic devices.

AUTHOR INFORMATION

Corresponding Author

Andrew M. Rappe − *Department of Chemistry, University of Pennsylvania, Philadelphia, Pennsylvania 19104−6323, United States;* ● orcid.org/0000-0003-4620-6496; Email: rappe@sas.upenn.edu

Authors

Lingyuan Gao − *Department of Chemistry, University of Pennsylvania, Philadelphia, Pennsylvania 19104−6323, United States;* ● orcid.org/0000-0001-8245-8880

Robert B. Wexler − *Department of Chemistry, University of Pennsylvania, Philadelphia, Pennsylvania 19104−6323, United States;* ● orcid.org/0000-0002-6861-6421

Ruixiang Fei − *Department of Chemistry, University of Pennsylvania, Philadelphia, Pennsylvania 19104−6323, United States*

Complete contact information is available at:
https://pubs.acs.org/10.1021/acs.jpcc.2c07844

Author Contributions

†These authors contributed equally to this work.

Notes

The authors declare no competing financial interest.

ACKNOWLEDGMENTS

REFERENCES

(1) Carruthers, J. R.; Peterson, G. E.; Grasso, M.; Bridenbaugh, P. M. Nonstoichiometry and Crystal growth of Lithium Niobate. *J. Appl. Phys.* **1971**, *42*, 1846−51.

(2) Nishihara, H.; Haruna, M.; Suhara, T. *Optical integrated circuits*; Electro-Optics Handbook; McGraw-Hill, 2000.

(3) Wooten, E. L.; Kissa, K. M.; Yi-Yan, A.; Murphy, E. J.; Lafaw, D. A.; Hallemeier, P. F.; Maack, D.; Attanasio, D. V.; Fritz, D. J.; McBrien, G. J.; et al. A review of lithium niobate modulators for fiber-optic communications systems. *IEEE J. Sel. Top. Quantum Electron.* **2000**, *6*, 69−82.

(4) Chen, F.; LaMacchia, J.; Fraser, D. *Landmark Papers on Photorefractive Nonlinear Optics*; World Scientific, 1995; pp 33−35.

(5) de Miguel-Sanz, E.; Carrascosa, M.; Arizmendi, L. Effect of the oxidation state and hydrogen concentration on the lifetime of thermally fixed holograms in LiNbO 3: Fe. *Phys. Rev. B* **2002**, *65*, 165101.

(6) Zhu, Y.-y.; Ming, N.-b. Ultrasonic excitation and propagation in an acoustic superlattice. *Journal of applied physics* **1992**, *72*, 904−914.

(7) Pruneri, V.; Koch, R.; Kazansky, P.; Clarkson, W.; Russell, P. S. J.; Hanna, D. 49 mW of cw blue light generated by first-order quasi-phase-matched frequency doubling of a diode-pumped 946-nm Nd: YAG laser. *Optics letters* **1995**, *20*, 2375−2377.

(8) Kösters, M.; Sturman, B.; Werheit, P.; Haertle, D.; Buse, K. Optical cleaning of congruent lithium niobate crystals. *Nat. Photonics* **2009**, *3*, 510−513.

(9) Schmidt, R.; Kaminow, I. Metal-diffused optical waveguides in LiNbO3. *Appl. Phys. Lett.* **1974**, *25*, 458−460.

(10) Arizmendi, L. Photonic applications of lithium niobate crystals. *physica status solidi (a)* **2004**, *201*, 253−283.

(11) Jackel, J. L.; Rice, C.; Veselka, J. Proton exchange for high-index waveguides in LiNbO3. *Appl. Phys. Lett.* **1982**, *41*, 607−608.

(12) Neyer, A.; Sohler, W. High-speed cutoff modulator using a Ti-diffused LiNbO3 channel waveguide. *Appl. Phys. Lett.* **1979**, *35*, 256−258.

(13) Fukuma, M.; Noda, J. Optical properties of titanium-diffused LiNbO 3 strip waveguides and their coupling-to-a-fiber characteristics. *Applied optics* **1980**, *19*, 591−597.

(14) Cabrera, J.; Olivares, J.; Carrascosa, M.; Rams, J.; Müller, R.; Diéguez, E. Hydrogen in lithium niobate. *Adv. Phys.* **1996**, *45*, 349−392.

(15) Rice, C. The structure and properties of Li1- xHxNbO3. *J. Solid State Chem.* **1986**, *64*, 188−199.

(16) Korkishko, Y. N.; Fedorov, V.; De Micheli, M.; Baldi, P.; El Hadi, K.; Leycuras, A. Relationships between structural and optical properties of proton-exchanged waveguides on Z-cut lithium niobate. *Applied optics* **1996**, *35*, 7056−7060.

(17) Korkishko, Y. N.; Fedorov, V. Structural and optical characterization of annealed proton exchanged LiNbO3 optical waveguides. *Opt. Mater.* **1996**, *5*, 175−185.

(18) Korkishko, Y. N.; Fedorov, V. A.; Katin, S.; Kondrat'ev, A. V. Reverse proton exchange in LiTaO$_3$ and LiNbO$_3$ for buried optical waveguides. Functional Photonic Integrated Circuits. *Proc. SPIE* **1995**, *2401*, 149−161.

(19) Korkishko, Y. N.; Fedorov, V. Structural phase diagram of H x/ Li 1-x NbO 3 waveguides: The correlation between optical and structural properties. *IEEE J. Sel. Top. Quantum Electron.* **1996**, *2*, 187−196.

(20) Korkishko, Y. N.; Fedorov, V.; Morozova, T.; Caccavale, F.; Gonella, F.; Segato, F. Reverse proton exchange for buried waveguides in LiNbO 3. *JOSA A* **1998**, *15*, 1838−1842.

(21) Ohsaka, T.; Kanzaki, Y.; Abe, M. Irreversible Li+/H+ ion-exchange reaction between cubic HNbO3 and rhombohedral LiNbO3 and NMR study of LixH1- xNbO3. *Materials research bulletin* **2001**, *36*, 2141−2154.

(22) Fedorov, V. A.; Korkishko, Y. N. Crystal structure and optical properties of proton-exchanged lithium niobate waveguides. Integrated Optics and Microstructures II. *Proc. SPIE* **1994**, *2291*, 243−255.

(23) Fedorov, V. A.; Korkishko, Y. N. Relationships between crystal lattice parameters and optical properties of proton-exchanged lithium niobate waveguides. Functional Photonic Integrated Circuits. *Proc. SPIE* **1995**, *2401*, 216−226.

(24) Korkishko, Y. N.; Fedorov, V. A.; Nosikov, V. V.; Kostritskii, S. M.; De Micheli, M. P. Phase diagram of $H_xLi_{1-x}NbO_3$ optical waveguides. Integrated Optics Devices: Potential for Commercialization. *Proc. SPIE* **1997**, 188−200.

(25) Rice, C.; Jackel, J. $HNbO_3$ and $HTaO_3$: New cubic perovskites prepared from $LiNbO_3$ and $LiTaO_3$ via ion exchange. *J. Solid State Chem.* **1982**, *41*, 308−314.

(26) Fourquet, J.; Renou, M.; De Pape, R.; Theveneau, H.; Man, P.; Lucas, O.; Pannetier, J. $HNbO_3$: structure and NMR study. *Solid State Ionics* **1983**, *9*, 1011−1013.

(27) Pokrovskii, L. Formation of the $HNbO_3$ phase by high-temperature annealing of $LiNbO_3$ substrates. *Journal of Structural Chemistry* **2000**, *41*, 890−894.

(28) Kalabin, I.; Grigorieva, T. I.; Pokrovsky, L. D.; Atuchin, V. V. Precipitation of $HNbO_3$ at the $Ti:LiNbO_3$ surface. *Integrated Optical Devices: Fabrication and Testing*; Society of Photo Optical, 2003; pp 140−145.

(29) Weller, M.; Dickens, P. Proton motion in $HNbO_3$ and $HTaO_3$. *J. Solid State Chem.* **1985**, *60*, 139−144.

(30) Giannozzi, P.; et al. Quantum ESPRESSO: A modular and open-source software project for quantum simulations of materials. *J. Phys.: Condens. Matter* **2009**, *21*, No. 395502.

(31) Rappe, A. M.; Rabe, K. M.; Kaxiras, E.; Joannopoulos, J. D. Optimized Pseudopotentials. *Phys. Rev. B Rapid Comm.* **1990**, *41*, 1227−1230.

(32) Perdew, J. P.; Burke, K.; Ernzerhof, M. Generalized Gradient Approximation Made Simple. *Phys. Rev. Lett.* **1996**, *77*, 3865.

(33) Bravais, A. *Etudes Crisfallographiques*; Gauthier-Villars: Paris, 1866.

(34) Donnay, J.; Harker, D. *Am. Mineral.* **1937**, *22*, 446.

(35) Friedel, G. *Bull. Soc. Franc. Mineral* **1907**, *07*, 326.

(36) Gonze, X.; Lee, C. Dynamical matrices, Born effective charges, dielectric permittivity tensors, and interatomic force constants from density-functional perturbation theory. *Phys. Rev. B* **1997**, *55*, 10355−68.

(37) Veithen, M.; Ghosez, P. First-principles study of the dielectric and dynamical properties of lithium niobate. *Phys. Rev. B* **2002**, *65*, 214302−12.

(38) Rohlfing, M.; Louie, S. G. Electron-Hole Excitations and Optical Spectra from First Principles. *Phys. Rev. B* **2000**, *62*, 4927−4944.

(39) Zelmon, D.; Small, D.; Jundt, D. Infrared corrected Sellmeier coefficients for congruently grown lithium niobate and 5 mol. *JOSA B* **1997**, *14*, 3319−3322.

🕮 Recommended by ACS